Zhou *et al. Journal of Nanobiotechnology* (2025) 23:243
https://doi.org/10.1186/s12951-025-03309-x

Journal of Nanobiotechnology

RESEARCH **Open Access**

Single-atom Zr doped heterojunction enhanced piezocatalysis for implant infection therapy through synergistic metal immunotherapy with sonodynamic and physical puncture

Xing Zhou[1,2,9†], Jingbo Xie[5,6†], Xingchen Zhou[1,2†], Tianyou Ma[1,2†], Yichen Lu[1,2], Yiwen Yang[1,2], Zhefei Xie[1,2], Houfu Ling[1,2], Rui Xu[3], Mo Wu[1,2], Jinglei Wang[1,2], Weixiang Wang[1,2], Derong Kong[4], Pengchao Xu[1,2], Xuan Wan[3,7], Hongbo Wu[8*], Peijian Tong[1,2*] and Hanting Xia[1,2,3*]

Abstract

Recent common clinical treatments for implant bacterial infections involve replacing inert implants and using antibiotics. However, these methods remain limited in their effectiveness for pathogen clearance, immune regulation, and osteogenesis. In this study, we developed a Zr-doped heterointerface of $SrTiO_3$ and Hap ($SrTiZrO_3$/Hap) heterojunction coating with single-atom Zr doping and heterogeneous interfaces designed for ultrasound-responsive antimicrobial activity and bone formation. Under ultrasound, the mechanical force exerted by $SrTiZrO_3$/Hap enhances its physical puncture and sonodynamic activity, synergizing with the metalloimmunotherapy effect of Zr^{4+} for efficient antimicrobial activity. The primary mechanism enhancing sonodynamic activity involves local interfacial polarization from single-atom Zr doping, achieving piezoelectric catalysis in conjunction with electronic polarization from the built-in electric field. $SrTiZrO_3$/Hap achieved a 99.3% antibacterial rate against *S. aureus* and 99.7% against *E. coli* under ultrasound. Additionally, $SrTiZrO_3$/Hap promoted osteogenic differentiation after ultrasound irradiation by activating the PI3K/Akt pathway *via* its piezoelectric, needle-like topological surface and the release of functional ions, thus accelerating bone repair.

Keywords Piezocatalysis, Sonodynamic therapy, Metalloimmunotherapy, Antibacterial, Bone formation

---

[†] Xing Zhou, Jingbo Xie, Xingchen Zhou and Tianyou Ma contributed equally to this work.

*Correspondence:
Hongbo Wu
wuhongbo@gzhmu.edu.cn
Peijian Tong
tongpeijian@163.com
Hanting Xia
xiahanting@zcmu.edu.cn

Full list of author information is available at the end of the article

Graphical abstract

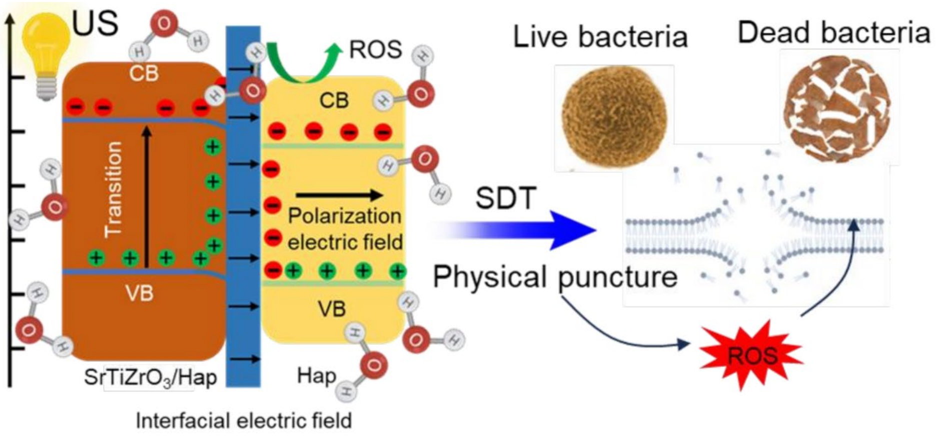

Introduction

Bacterial infection of implants is a condition in which bone tissue becomes infected and damaged, leading to abscesses within the marrow cavity and the formation of bone defects [1–9]. Common causes include traumatic infections, surgical complications, and hematogenous infections [10–12]. Traditional treatments, including surgical debridement, antibiotic therapy, and bone grafting, have some limitations and side effects [13–15]. For example, surgical debridement can lead to poor wound healing and bone tissue re-injury; antibiotics treatment may cause resistant bacterial strains and systemic side effects, and bone grafting often faces donor shortages and rejection risks [16–18]. Consequently, discovering new treatment methods remains a challenge for current research. Clinical bone defects frequently carry risks of primary or secondary infections. Thus, an ideal bone repair coating material should offer both excellent osteogenic and antimicrobial properties [19, 20].

Exogenously responsive antimicrobial methods, including visible light, near-infrared light (NIR), ultrasonic (US), and microwave, have recently gained increasing attention [21–23]. Currently, commonly used photosensitizers are inorganic nanomaterials, which generate photothermal effects and photogenerated electrons by absorbing visible light or NIR, converting it into reactive oxygen species (ROS) and high heat temperatures. Consequently, the synergistic photodynamic and photothermal effects swiftly eliminate bacteria [24]. The weak penetration of light can lead to insufficient antimicrobial properties in vivo; therefore, antimicrobial treatments with greater penetration depth are necessary [24, 25]. Compared with NIR light, the US possesses greater tissue penetration and biosafety, overcoming the drawbacks of photoactivation, phototoxicity, and shallow penetration depth, making it a potential therapeutic solution for bacterial infections in implants [26–29]. Like light, the US is also a means of energy transfer [30]. Then, designing US-responsive heterojunction composite coatings on implant surfaces for similar sonothermal and sonodynamic synergistic antimicrobial therapy is also theoretically possible [31–33]. Like phototherapy, US therapy is inevitably inseparable from sonosensitizers. Conventional sonosensitizers are mainly inorganic sonosensitizers (TiO_2 and MoS_2) and organic acoustic sensitizers (porphyrin-like compounds and rose bengal) [34, 35]. Among them, metal oxides (like ZnO) usually have good piezoelectric catalytic properties due to the asymmetry of their overall structure. In recent years, it has also emerged that the piezoelectric nature of ZnO is exploited to achieve the generation of a large number of free radicals under ultrasound to kill bacterial or tumour cells for antibacterial and anti-tumour sonodynamic therapeutic purposes [36–40]. However, compared with inorganic sonosensitizers, organic sonosensitizers have poor stability and pharmacokinetics in physiological environments, thus limiting their application in the antimicrobial field.

Strontium titanate ($SrTiO_3$), a traditional bioactive semiconductor material with a high bandwidth of approximately 3.2 eV, exhibits excellent photocatalytic activity, a large surface area, and abundant catalytic sites, making it widely used in photocatalytic degradation of organic pollutants and other applications [41, 42]. Its asymmetric structure enables piezoelectric activity for piezoelectric catalysis, which can generate ROS through electronic polarization under the US to achieve rapid antimicrobial process [43]. However, single $SrTiO_3$ exhibits poor US response antimicrobial activity, low US electron-hole pair separation efficiency, and high recombination efficiency, making it challenging to enhance its catalytic activity [43, 44]. Currently, the primary approach is doping or constructing heterogeneous interfaces to improve its piezoelectric performance, which can introduce new active sites and change the Fermi energy level of the composite interface to enhance the piezoelectric catalytic effect [45–47]. Additionally, hydroxyapatite (Hap), known for its osteogenic properties, has non-central symmetry that grants it certain piezoelectric performance [48, 49]. However, the piezoelectricity of Hap is weak due to the easily compounded properties of the US-excited electron-hole pairs, making it necessary to inhibit their compounded efficiency to improve its US response [50, 51].

To enhance the piezoelectric activity of $SrTiO_3$ and Hap under the US, We prepared exogenously responsive implant coatings by a multistep hydrothermal method, and compared to previous tubulin/kinesin active nematic gel, we achieved exogenously responsive and rapid treatment of infected bone defects. The introduction of single-atom Zr doping provides local interfacial polarization that can be enhanced under the US and, combined with electron polarization from the built-in electric field of the heterointerface, achieves a piezocatalysis effect for highly efficient treatment of implant bacterial infections (Scheme 1). Meanwhile, the needle-like surface topology of $SrTiZrO_3$/Hap can enhance antibacterial

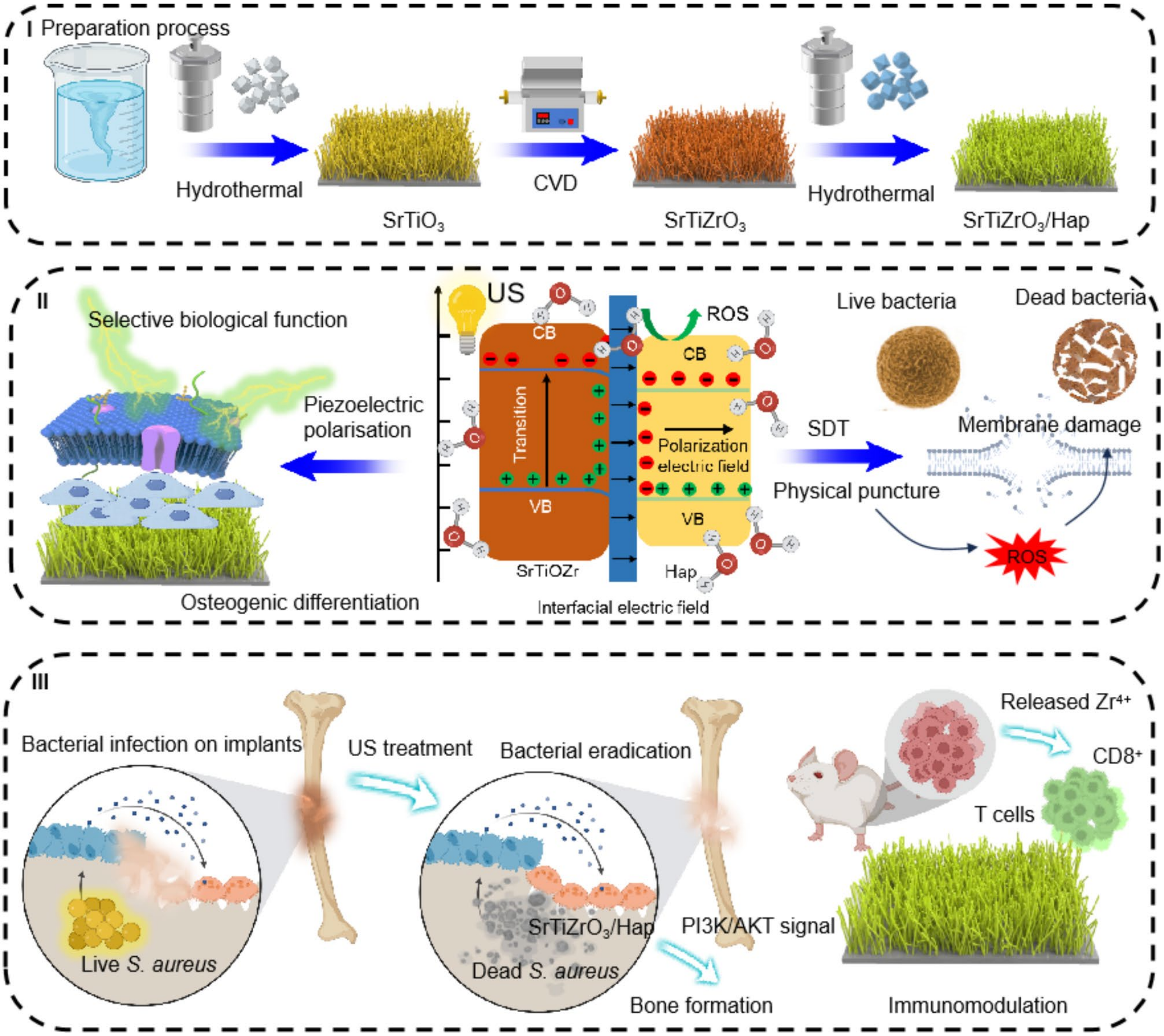

Scheme 1 The diagram of $SrTiZrO_3$/Hap preparation and the mechanism of antimicrobial activity under US and in vivo schematic for the treatment of implant bacterial infection

sonodynamic activity through physical puncture. The single-atom Zr-doped $SrTiZrO_3$/Hap releases Zr^{4+} to modulate immunity, enabling efficient and rapid bacterial clearance through physical puncture-enhanced sonodynamic therapy combined with metalloimmunotherapy. Under US irradiation, $SrTiZrO_3$/Hap produces more ROS compared with uncompounded $SrTiO_3$ and Hap. The antimicrobial rate of $SrTiZrO_3$/Hap was 99.3% against *S. aureus* and 99.7% against *E. coli*. US-inspired antimicrobial and osteogenic coatings are an emerging therapeutic strategy with multiple advantages of promoting bone healing, enhancing antimicrobial effects and improving repair. US can act directly on bacterial cells by generating mechanical fluctuations, cavitation effects and temperature changes, thereby disrupting the bacterial cell membranes and enhancing the bactericidal effect of antimicrobial coatings [52]. In addition, ultrasound can promote more effective penetration of antimicrobial agents into the lesion site, enhancing their local concentration and efficacy. By optimising the coating design and parameter modulation of ultrasound, this strategy has promising applications in orthopaedics, dentistry and other related fields. It also achieved effective bone repair and bacterial clearance in an in vivo rat model, demonstrating potential as a US-responsive antimicrobial and osteogenic coating for implant infections.

Results and discussion

The morphology and structural characteristics of the coatings were analyzed using scanning electron microscopy (SEM) and transmission electron microscopy (TEM). The substrate morphology, illustrated in Figure S1, exhibited a slightly rough surface. The $SrTiO_3$ coating was prepared on the titanium surface via a hydrothermal method, resulting in a needle-like regular structure (Fig. 1a). After Zr doping, the morphology remained unchanged, retaining the needle-like nanowire morphology (Fig. 1b). The Hap coating surface displayed homogeneous rod structures, while the $SrTiZrO_3$/Hap heterojunction coating exhibited a flat rod structure. The coating morphology presented a tiled, rod-like structure, similar to the single Hap structure (Fig. 1c-d). This structure can physically puncture the cell wall of bacteria and destroy their cellular structure, thus achieving the antibacterial effect. As for the cells contacted on its surface, its topology facilitates cell proliferation and differentiation, thus promoting the coating to contribute to the level of osteogenic differentiation and achieving the dual functions of antibacterial and osteogenic. To analyze the bonding between $SrTiZrO_3$ and Hap, TEM images of $SrTiZrO_3$ and $SrTiZrO_3$/Hap heterojunctions were analyzed before and after compounding. As displayed in Fig. 1e-f, TEM images of $SrTiZrO_3$ exhibited a needle-like structure approximately 320 nm in length, consistent with SEM observations. When combined with Hap, the rod-like structure of Hap interweaved with the nanoneedles of $SrTiZrO_3$. High-resolution TEM images revealed atomic-level contacts at the crystalline surfaces, with (001) and (002) planes corresponding to $SrTiZrO_3$ and Hap, respectively (Fig. 1f). Additionally, TEM elemental mapping of $SrTiZrO_3$/Hap revealed a uniform distribution of Zr, Ca, P, Sr, Ti, and O (Fig. 1g), confirming the formation of a uniform composite of $SrTiZrO_3$ and Hap on the substrate. Since the surface potential of $SrTiO_3$ is negative and that of Hap is opposite to it, Hap and $SrTiZrO_3$ are able to bond by electrostatic interaction when the i*n-situ* growth of Hap is carried out on the surface of the $SrTiO_3$-doped coating [53, 54]. Figure 1h presents the XRD curves of different coatings. Both $SrTiO_3$ and $SrTiZrO_3$ samples exhibited distinct diffraction peaks of $SrTiO_3$ at 36.1°, corresponding to the (001) crystallographic facet of $SrTiO_3$. Similarly, Hap and $SrTiZrO_3$/Hap samples displayed Hap crystal diffraction peaks at 31.9°, matching the (002) crystallographic facet of Hap. These crystal faces in Hap, $SrTiO_3$, and $SrTiZrO_3$/Hap confirmed successful preparation on the substrate.

XPS (X-ray photoelectron spectroscopy) spectra were obtained to analyze the elemental compositions of $SrTiO_3$, $SrTiZrO_3$, Hap, and $SrTiZrO_3$/Hap. As displayed in Fig. 1i, the elements Ca, P, and Sr were not detected in the substrate samples. Sr, Zr, and Ti were observed in both $SrTiZrO_3$ and $SrTiZrO_3$/Hap, while Ca and P were detected in Hap and $SrTiZrO_3$/Hap, confirming the successful composite of $SrTiZrO_3$ and Hap. High-resolution XPS spectra further clarified the elemental compositions of $SrTiZrO_3$, Hap, and $SrTiZrO_3$/Hap. To verify Zr atom doping in $SrTiO_3$, synchrotron radiation detection was performed. Figure 1j and k illustrate that Zr-O bonds are present in $SrTiZrO_3$/Hap but not in ZrO_2, which has both Zr-O and Zr-Zr bonds. This suggests that the doped Zr is mainly monoatomic. The distributions of Ca 2p, Sr 3d, and Zr 2d, illustrated in Figures S1, match the total XPS spectra, further confirming the successful preparation of $SrTiZrO_3$, Hap, and $SrTiZrO_3$/Hap coatings on the implant surface.

As shown in Figure S2, we then examined the UV-Vis absorption spectra of $SrTiZrO_3$/Hap, and the results showed that the different samples had good light-absorbing properties in the visible light band. Moreover, after compositing, we found that the light absorption performance of the composite group $SrTiZrO_3$/Hap was enhanced compared with that of the uncomposite group, which was mainly due to the construction of the heterogeneous interface that provided a large number of light reflection sites and greatly improved the light absorption of $SrTiZrO_3$/Hap. The effect of single-atom Zr doping and its combination with Hap on the energy band structure of $SrTiZrO_3$/Hap was analyzed using XPS valence

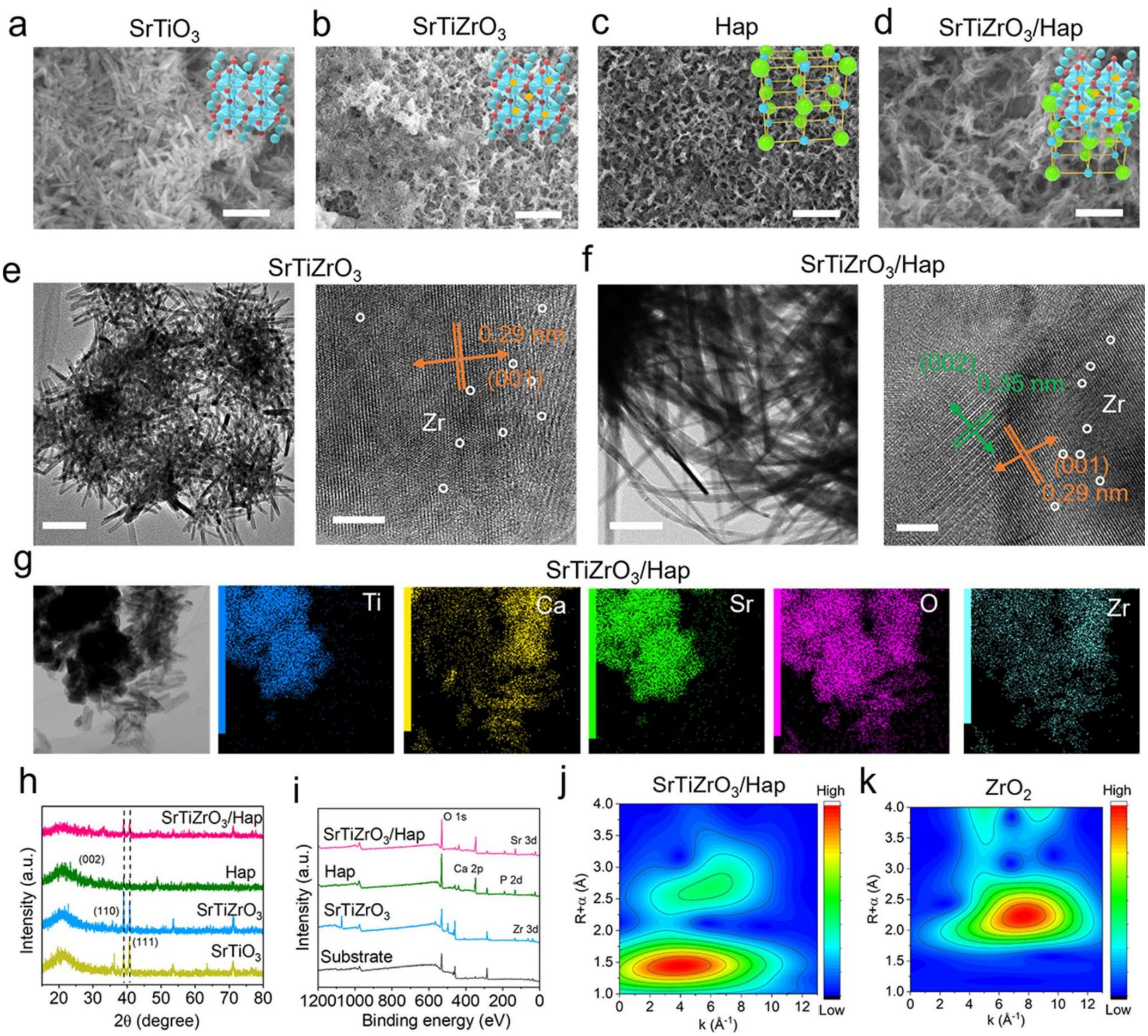

Fig. 1 **a**-**b**, SEM image of $SrTiO_3$ and $SrTiZrO_3$ coating, scale bar was 200 nm; **c**-**d**, SEM image of Hap coating and $SrTiZrO_3$/Hap coating, scale bar was 200 nm; **e**-**f**, low magnification and high magnification TEM images of $SrTiZrO_3$ and $SrTiZrO_3$/Hap, scale bar was 200 nm (low magnification) and 5 nm (high magnification); **g**, element mapping images of $SrTiZrO_3$/Hap; **h**, XRD spectra of $SrTiO_3$, $SrTiZrO_3$, Hap, and $SrTiZrO_3$/Hap; **i**, XPS spectra of different samples; **j**-**k**, wavelet analytical images of $SrTiZrO_3$/Hap and ZrO_2

band spectra. As presented in Fig. 2a–d, the valence band positions of $SrTiO_3$, $SrTiZrO_3$, Hap, and $SrTiZrO_3$/Hap were 2.38, 2.64, 2.51, and 1.68 eV, respectively. These results revealed that the valence band position of $SrTiO_3$ decreased after Zr single atom doping, and the valence band of $SrTiZrO_3$/Hap was lower than that of uncompounded $SrTiZrO_3$. To analyze the sonodynamic properties of $SrTiZrO_3$/Hap, piezoelectric properties were measured using piezo force microscopy (PFM). $SrTiO_3$, $SrTiZrO_3$, Hap, and $SrTiZrO_3$/Hap each exhibited a degree of piezoelectric polarization, resulting in a surface potential (Fig. 2e–h). Meanwhile, we can find that the piezoelectric activity of $SrTiZrO_3$ was better than $SrTiO_3$ because of higher surface piezoelectric potential. As displayed in Fig. 2i-j, the piezoelectric potential of both $SrTiO_3$ and $SrTiZrO_3$/Hap increased after US irradiation, with $SrTiZrO_3$/Hap exhibiting a higher potential than $SrTiO_3$ due to its stronger piezoelectricity. As illustrated in Fig. 2k–n, the butterfly curves and phase images of $SrTiZrO_3$/Hap and $SrTiO_3$ demonstrate that single-atom Zr doping and the construction of heterogeneous interfaces between $SrTiZrO_3$ and Hap can significantly enhance the piezoelectric effect. After applying in situ US irradiation, $SrTiZrO_3$/Hap exhibited a significant increase in surface potential, indicating dielectric polarization generation.

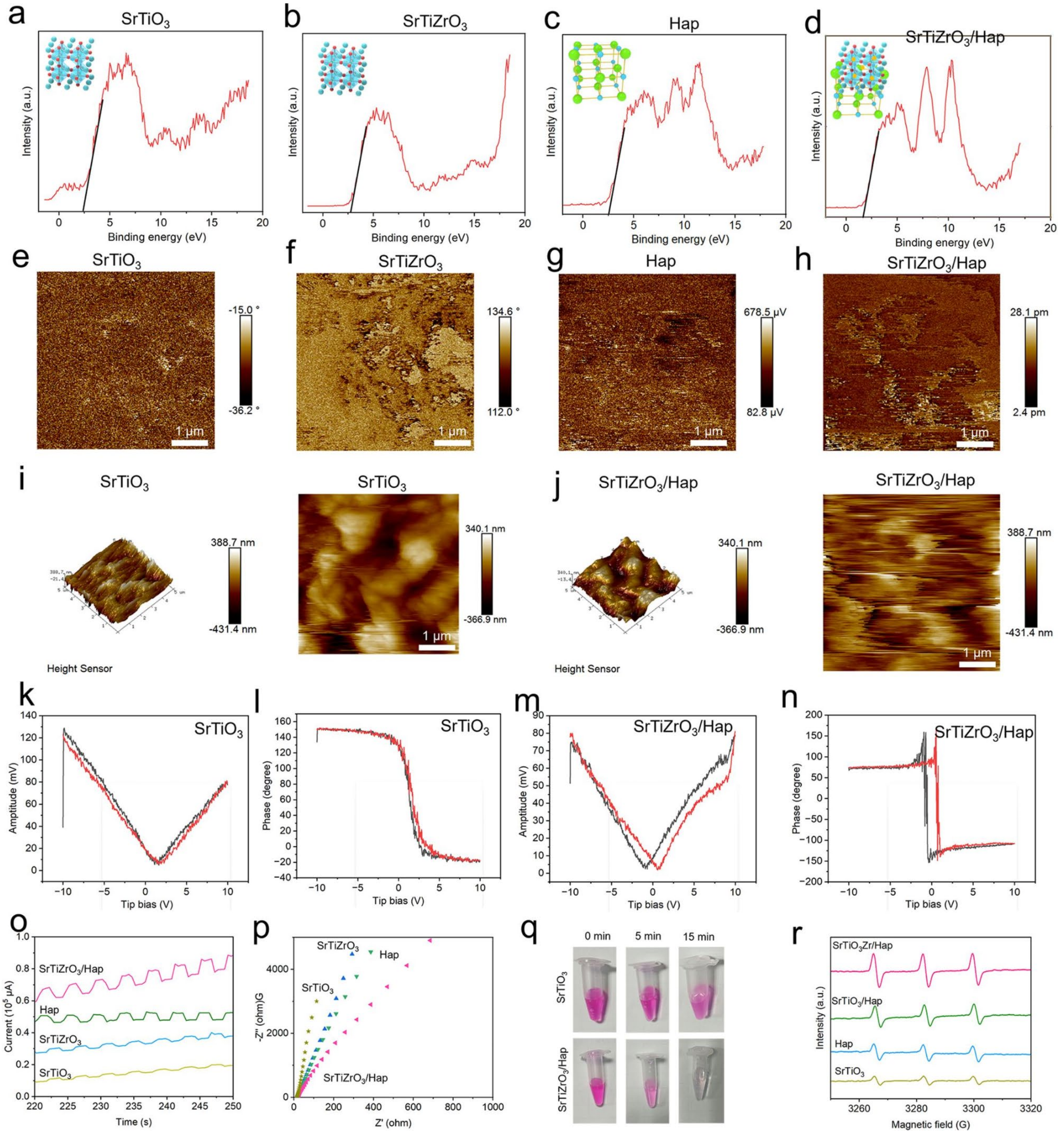

Fig. 2 **a**-**d**, valence band spectra of $SrTiO_3$, $SrTiZrO_3$, Hap, and $SrTiZrO_3$/Hap; **e**-**h**, PFM detection of $SrTiO_3$, $SrTiZrO_3$, Hap, and $SrTiZrO_3$/Hap; **i**-**j**, in-situ PFM images of $SrTiO_3$ and $SrTiZrO_3$/Hap after US irradiation; **k**-**l**, amplitude curve and butterfly curve of $SrTiO_3$; **m**-**n**, amplitude curve and butterfly curve of $SrTiZrO_3$/Hap; **o**-**p**, I-t and impedance curves of $SrTiO_3$, $SrTiZrO_3$, Hap and $SrTiZrO_3$/Hap after US excitation; **q**, efficiency of degradation of RhB by $SrTiO_3$ and $SrTiZrO_3$/Hap under US irradiation; **r**, ESR curves of $SrTiZrO_3$/Hap of $SrTiO_3$, $SrTiZrO_3$, Hap and $SrTiZrO_3$/Hap after US irradiation

The US, combined with in situ electrochemistry, was used to examine the piezoelectric catalytic performance of $SrTiZrO_3$/Hap visually. As illustrated in Fig. 2o-p, the US current of $SrTiZrO_3$/Hap increased by more than 1.2-fold compared with $SrTiZrO_3$ and Hap after compounding, while the US current of unmodified $SrTiO_3$ remained weaker and insufficient to generate a substantial current under the US. Electrochemical impedance results indicated that $SrTiZrO_3$/Hap exhibited lower impedance, resulting in the highest US electron transfer efficacy and the lowest electron-hole pair complexation efficiency. The degradation of RhB after US irradiation accounted for the piezoelectric effect in different samples. As illustrated in Fig. 2q, the US alone did not degrade RhB, indicating that it did not exhibit catalytic behavior. The degradation rate of $SrTiZrO_3$/Hap after the US was significantly faster than that of $SrTiO_3$, suggesting that compounding enhanced the US response and piezoelectric properties of $SrTiZrO_3$/Hap, leading to improved RhB degradation performance. To analyze the ROS generation performance of $SrTiZrO_3$/Hap under US, we subsequently examined the sonodynamic properties of different samples using electron spin resonance (ESR). As displayed in Fig. 2r, after 10 min US irradiation, $SrTiZrO_3$/Hap exhibited clear ROS production, indicating a substantial generation of $\cdot\ ^1O_2$. As shown in Figure S3, we found that Zr doping can enhance ROS production compared with SrTiO3/Hap about 1.23 fold, it indicated that Zr doping was beneficial for sonodynamic antibacterial therapy. According to our derived energy band positions of $SrTiZrO_3$/Hap, its potential position was higher than that required for superoxide production, and thus when free electrons are produced by $SrTiZrO_3$/Hap under the action of ultrasound, the unneutralised electrons from the holes are able to react rapidly with the surrounding O_2 and simultaneously generate a large amount of superoxide, achieving excellent sonodynamic activity [55].

The mechanism behind the enhanced piezoelectric performance of $SrTiZrO_3$/Hap was investigated using DFT (density functional theory) calculation. The structures of $SrTiZrO_3$, Hap, and $SrTiZrO_3$/Hap were shown in Fig. 3a-c, respectively. Both $SrTiZrO_3$ and Hap were tightly combined by bonding cooperation after the composite, and the structures may be favorable for charge transport by US excitation. In this case, after we constructed the two as a heterojunction, the two as a whole showed a composite structure, forming an ionic bond. After sonication, the crystal structure does not change, thus we are able to analyze the electronic behavior of the heterojunction after sonication. As illustrated in Fig. 3b–e, the density of electronic states analysis indicated that $SrTiZrO_3$/Hap heterojunction exhibited metallic characteristics at the Fermi energy level. Enhanced electrical conductivity. The electron cloud contributed by Ti was the highest, indicating its highest free electron contribution at the interface. From the DOS plots of the $SrTiZrO_3$/Hap structure, we can find that the DOS near the Fermi energy level is mainly contributed by the Ti, Sr and O orbitals, and that the DOS of Ti is the largest, which represents the most significant contribution of its electron cloud near the Fermi surface, and that the contribution of the electron cloud of its s orbital appears in the lower energy range, while that of the d orbital appears in the higher energy range [56]. For the DOS of $SrTiZrO_3$/Hap and $SrTiO_3$/Hap, we can find a decrease in the contribution of the O element near the Fermi surface, which also indicates the elevated contribution of the Ti element near the Fermi surface. After the combination, Zr also supplied electron orbitals at the interface, accelerating the US catalytic process. Differential charge density analysis was then performed. We then compared differential charge density before and after applying US. As displayed in Fig. 3f, after contact in the heterojunction, more free electrons were present at the interface, with electron flow directed from Hap to $SrTiZrO_3$. The differential charge density of the heterostructures also increased after the US. A comparison of the differential charge densities between $SrTiO_3$/Hap and $SrTiZrO_3$/Hap indicated that single-atom Zr doping enhanced electron flow at the interface, suggesting that Zr doping can synergistically boost the piezoelectric catalytic activity of the heterojunction. To further investigate the Fermi energy levels before and after the interaction between $SrTiZrO_3$ and Hap, we calculated the work functions (W_f) of $SrTiZrO_3$ and $SrTiZrO_3$/Hap before and after US using DFT analysis. As illustrated in Fig. 3g, W_f increased after the US, indicating a decrease in the Fermi energy level. Upon contact between $SrTiZrO_3$ and Hap, interface carriers were redistributed due to the different Fermi energy levels of the two. Low-intensity US induced mechanical deformation and a piezoelectric effect in $SrTiZrO_3$ with Hap, which triggered electron-hole pairs generation. A semiconductor heterojunction formed at the interface of $SrTiZrO_3$ and Hap, resulting in energy band bending that facilitated the separation and migration of electron-hole pairs. Hap, as a semiconductor, is able to form a heterogeneous interface after contacting with $SrTiZrO_3$, accepting free electrons from $SrTiZrO_3$ excitation, which improves the yield of US-generated electrons in the heterojunction, and increases the transfer efficiency of the electron-hole pairs to improve the piezocatalytic efficiency. Zr doping on the one hand can improve the interfacial polarization of $SrTiO_3$ and its piezoelectric responsiveness; at the same time, under the action of ultrasound can provide a part of the impurity energy level as well as increase the reactive sites of the reaction system, thus increasing the transfer efficiency of electron-hole pairs and decreasing the complexation process of electron-hole pairs. The effect of ultrasonication on the electron-hole pairs can be improved.

Therefore, the mechanism behind the enhanced US catalytic performance of the $SrTiZrO_3$/Hap complex primarily involves the electron transfer process at the interface. Upon contact between $SrTiZrO_3$ and Hap, an internal electric field was established, bending the band structure. This improved the transfer efficiency of electron-hole pairs, suppressed the compounding efficiency, and increased the number of free electrons involved in the ROS, ultimately enhancing sonodynamic

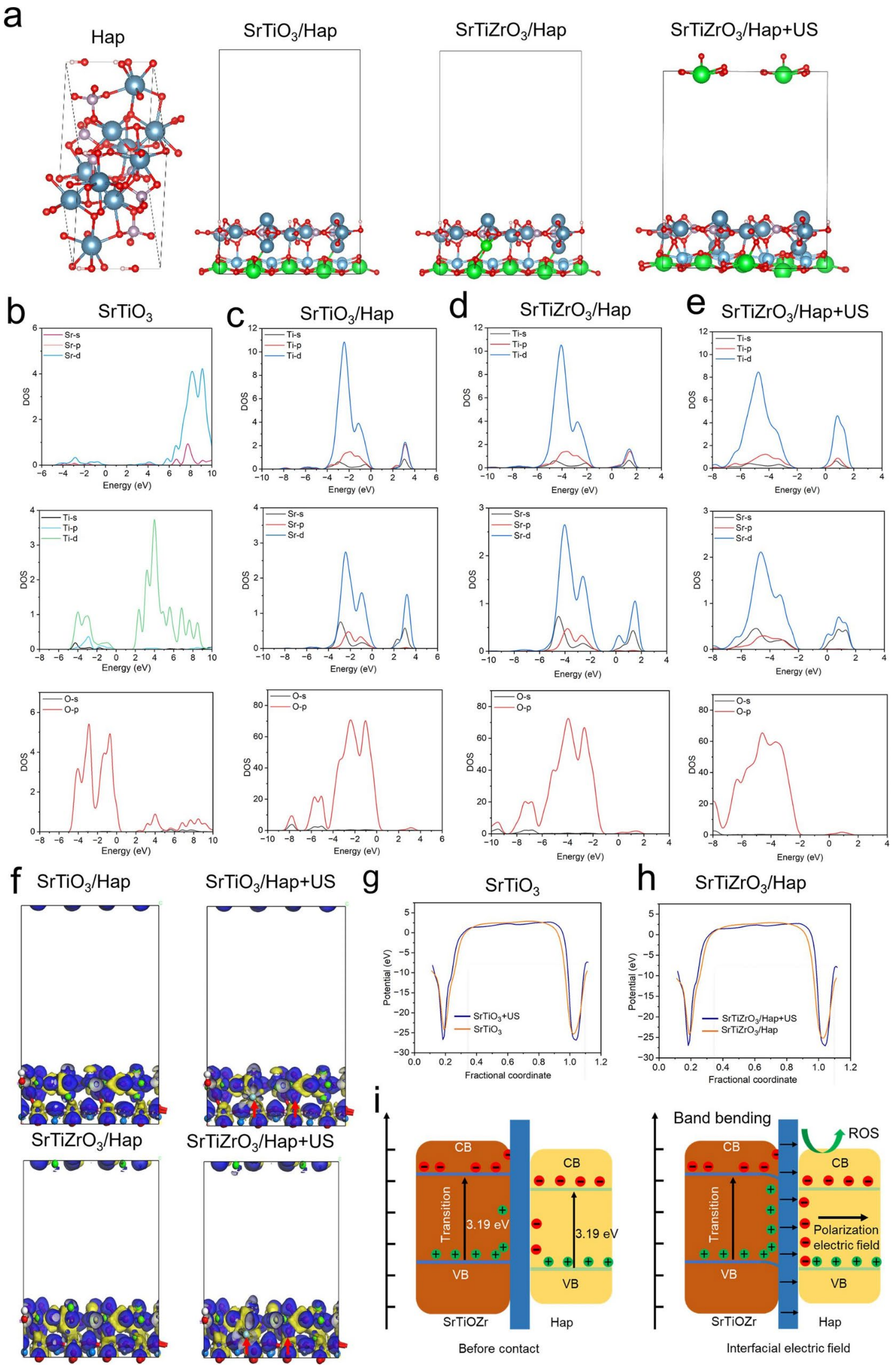

Fig. 3 **a**, schematic crystal structures of Hap, $SrTiO_3$/Hap and $SrTiZrO_3$/Hap; **b**, electron density of states of $SrTiO_3$; **c**, electron density of states of $SrTiO_3$/Hap; **d**, electron density of states of $SrTiZrO_3$/Hap; **e**, electron density of states plots of $SrTiZrO_3$/Hap + US; **f**, electron density of states of $SrTiO_3$/Hap and $SrTiZrO_3$/Hap differential charge density images before and after stress; **g**-**h**, W_f of $SrTiO_3$ and $SrTiZrO_3$/Hap before and after US irradiation; **i**, the piezocatalytic mechanism of $SrTiZrO_3$/Hap coating

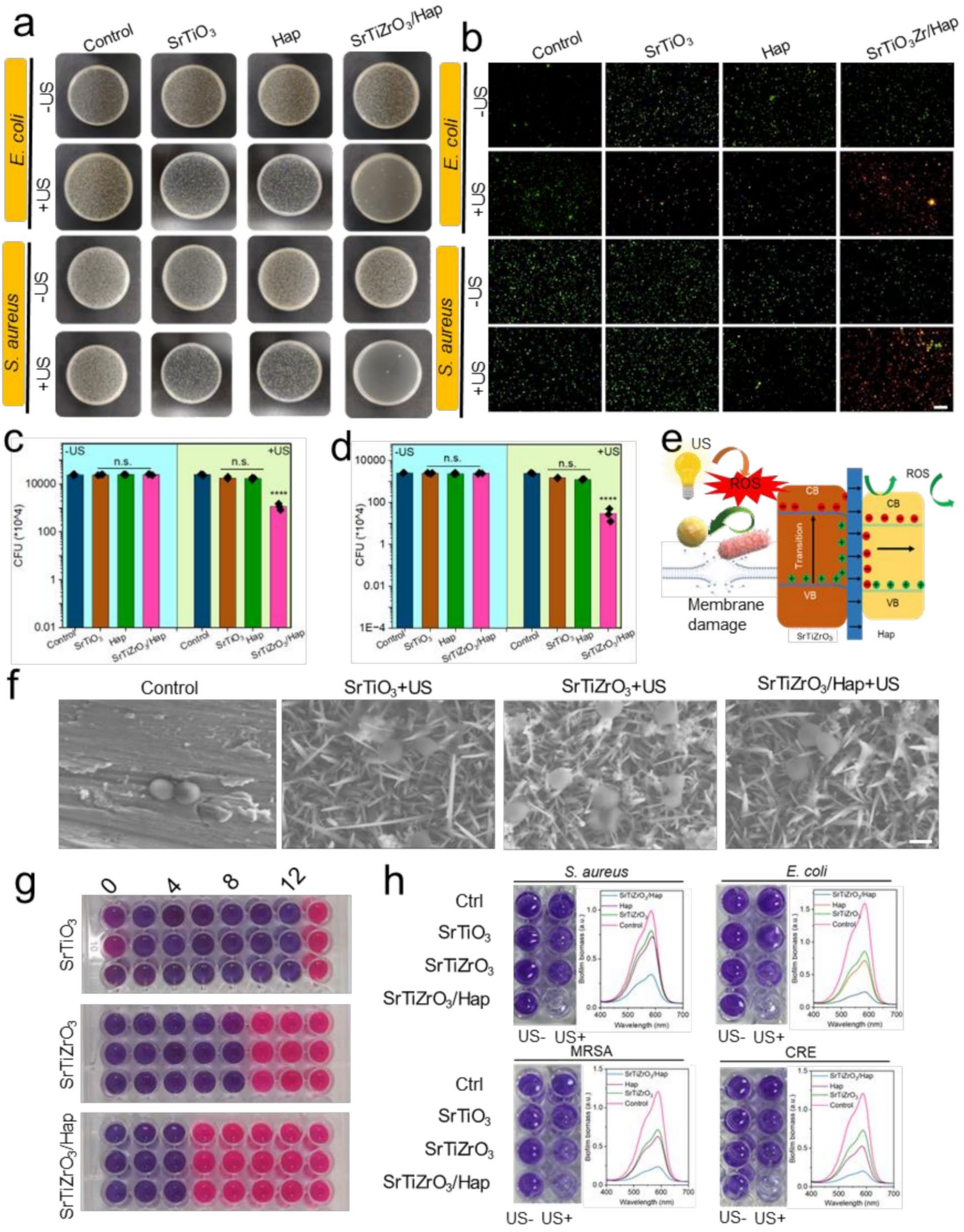

Fig. 4 (See legend on next page.)

(See figure on previous page.)

Fig. 4 **a**-**b**, spread plate and bacterial fluorescence images of $SrTiO_3$, $SrTiZrO_3$, Hap and $SrTiZrO_3$/Hap for *S. aureus* and *E. coli* with and without US irradiation, scale bar = 20 μm; **c**-**d**, bacterial survival rate of $SrTiO_3$, $SrTiZrO_3$, Hap and $SrTiZrO_3$/Hap for *S. aureus* (left) and *E. coli* (right); **e**, schematic of $SrTiZrO_3$/Hap antibacterial under US; **f**, SEM images of different samples after treating the bacteria without US, scale bar = 1 μm; **g**, bacterial Resazurin staining images of $SrTiZrO_3$/Hap after different incubation time (2 h, 4 h, 6 h, 8 h, 10 h, 12 h, 14 h); **h**, the biofilm images and corresponding absorbance spectra of *S. aureus*, *E. coli*, MRSA, and CRE

performance (Fig. 3i). Based on the results of the sonodynamic properties, $SrTiZrO_3$/Hap demonstrated excellent sonodynamic properties under US irradiation. To further evaluate its antimicrobial ability, we tested the antimicrobial efficacy of $SrTiZrO_3$/Hap against *S. aureus* and *E. coli* by co-culturing different coatings with the bacteria and sonicating for 12 min or keeping them in the dark for 12 min. As illustrated in Fig. 4a-b, no antimicrobial effect was observed in the co-culture of samples and bacteria across different groups. However, $SrTiZrO_3$ and Hap demonstrated antimicrobial efficiencies of 26.1% and 30.2% against *S. aureus* after US irradiation, respectively, while $SrTiZrO_3$/Hap achieved a high antimicrobial efficiency of 99.3%. For *E. coli* strains, $SrTiO_3$ and Hap demonstrated antimicrobial efficiencies of 39.4% and 48.6%, respectively, while $SrTiZrO_3$/Hap reached 99.7%. The quantitative results from the spread plate assay confirmed this result, with $SrTiZrO_3$/Hap exhibiting the highest antibacterial activity against both *S. aureus* and *E. coli* (Fig. 4c-d). We then performed live/dead bacterial fluorescence characterization. As illustrated in Fig. 4b, no dead bacteria were observed in the Control group before and after US irradiation. Similarly, $SrTiZrO_3$ and Hap did not exhibit significant antibacterial properties before the US, only killing a small number of bacteria during sonication. Conversely, the $SrTiZrO_3$/Hap group effectively killed most of the bacteria, demonstrating a significant improvement in antimicrobial efficiency compared with $SrTiZrO_3$ and Hap. This was mainly due to the excellent sonodynamic ability under US irradiation; $SrTiZrO_3$/Hap rapidly generated active US-excited electrons that reacted with O_2 in the solution to produce ROS, thus achieving excellent antibacterial effects (Fig. 4e). Due to the limited piezocatalytic ability of $SrTiZrO_3$ and Hap, their antimicrobial efficiency was lower compared with the $SrTiZrO_3$/Hap group. Considering that the needle-like structure of $SrTiZrO_3$ may exert a physical piercing effect on bacteria, we continued the co-culture of $SrTiZrO_3$ with bacteria following US irradiation. SEM images of bacteria revealed damage to the bacterial structure after the co-culturing, with needle tips penetrating the bacteria, indicating that $SrTiZrO_3$ can generate antimicrobial properties through this physical piercing effect. Whereas the morphology of the bacteria treated in the Control group without US showed a better round ball shape, the surface bacterial activity was not disturbed by US, and this result is also consistent with the plate spread and the live-dead fluorescence staining of the bacteria (Figure S4). $SrTiZrO_3$/Hap coating needle-like structure not only increased the surface roughness, which improved the chance of bacterial contact, but also the tip structure was able to puncture the bacteria under ultrasound, so that the bacterial membrane will be punctured, which will lead to the leakage of its internal contents, thus leading to the death of the bacteria. This result was also confirmed by bladed azure staining (Fig. 4g).

Furthermore, the antimicrobial effect of $SrTiZrO_3$ was more significant after US irradiation, indicating that the US could enhance the piercing effect through its mechanical action. The continuous stress of US can make $SrTiZrO_3$ more effective at disrupting the membrane structure of bacteria, thus enhancing its antibacterial properties through sonodynamic effects synergized with physical puncture (Fig. 4h). ROS were able to attack unsaturated fatty acids in bacterial cell membranes, triggering lipid peroxidation. In this process, ROS lead to the oxidation of fatty acids and the formation of hydroperoxides, which in turn can be further decomposed to produce more ROS, forming a continuous oxidative cycle that ultimately leads to cell membrane damage and destruction [57]. Subsequently, we analyzed the effect of $SrTiZrO_3$/Hap on biofilm removal under US. The cationic nature of the crystalline violet dye in solution allows it to bind to components of the biofilm by electrostatic forces, thus giving a more prominent purple colouration for the more biofilm-rich subgroups, whereas the more antimicrobial $SrTiZrO_3$/Hap group was able to give a lower purple staining. As illustrated in Fig. 4i, $SrTiZrO_3$, Hap, and $SrTiZrO_3$/Hap exhibited no significant antibiofilm effect in the absence of US stimulation. However, under US, it was observed that $SrTiZrO_3$ and Hap were able to remove 30–50% of the biofilm, although they did not achieve high efficiency in biofilm removal. However, $SrTiZrO_3$/Hap demonstrated excellent removal effects against *S. aureus*, *E. colii*, MRSA (Methicillin-resistant Staphylococcus aureus), and CRE (Carbapenem-resistant enterobacteriaceae bacteria), suggesting that $SrTiZrO_3$/Hap can remove biofilms on their surfaces effectively. We conducted several repetitions of ultrasound-responsive antimicrobial tests in order to evaluate the durability of the $SrTiZrO_3$/Hap coatings, and based on the results, we found that our $SrTiZrO_3$/Hap coatings still possessed an excellent antimicrobial effect after 200 min of ultrasonic irradiation instantly, which demonstrated the excellent durability of the $SrTiZrO_3$/Hap coatings (Figure S5).

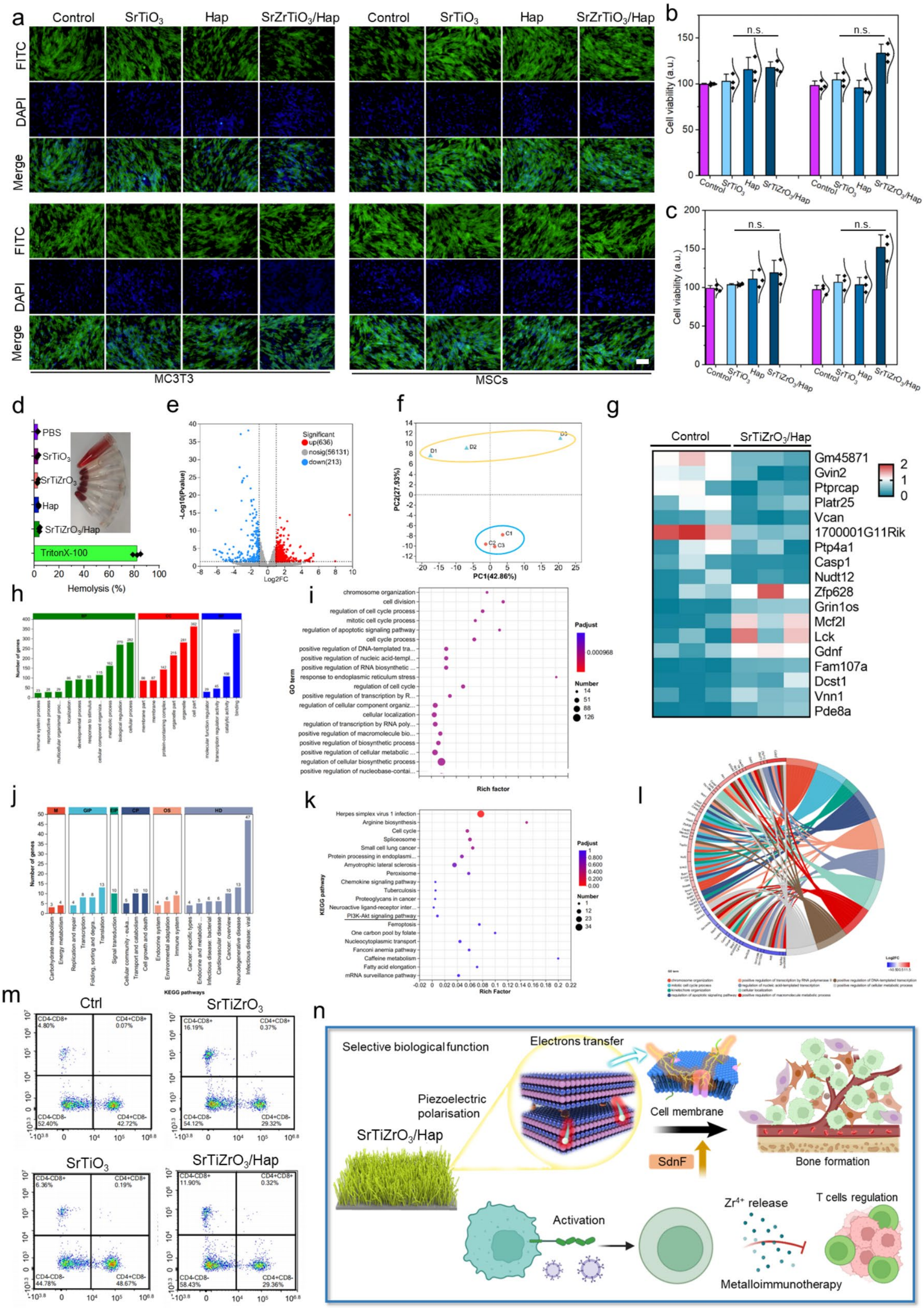

Fig. 5 (See legend on next page.)

(See figure on previous page.)

Fig. 5 **a**, cellular activities of Control, $SrTiO_3$, Hap and $SrTiZrO_3$/Hap for MC3T3 and MSCs cells after 1 and 3 Day incubation, scale bar = 20 μm; **b**-**c**, MC3T3 and MSCs cellular activities of Control, $SrTiO_3$, Hap and $SrTiZrO_3$/Hap for MC3T3 cells after 1 and 3 Day incubation; **d**, hemolysis of $SrTiO_3$, $SrTiZrO_3$, Hap, and $SrTiZrO_3$/Hap; **e**, differential gene volcano maps of Control and $SrTiZrO_3$/Hap for regulation of MSCs cells; **f**-**g**, PCA analysis and heat map of Control and $SrTiZrO_3$/Hap for MSCs after US irradiation; **h**-**i**, Control and $SrTiZrO_3$/Hap for differential gene GO enrichment analysis after US irradiation of MSCs; **j**-**l**, Control and $SrTiZrO_3$/Hap for differential gene KEGG enrichment analysis and enriched chordal plots after US irradiation of MSCs differential gene KEGG enrichment analysis; **m**, flow analysis of the infected tissues of Control, $SrTiO_3$, Hap and $SrTiZrO_3$/Hap after 2 D treatment; **n**, the bone formation mechanism of $SrTiZrO_3$/Hap coating by US irradiation

We then analyzed the cytotoxicity of $SrTiO_3$, $SrTiZrO_3$, Hap, and $SrTiZrO_3$/Hap and corresponding cell-regulated behaviors. As illustrated in Fig. 5a, none of the samples exhibited significant cytotoxicity after 1 and 3 days of co-culture with MC3T3-E1 and MSCs cells. Furthermore, both Hap and $SrTiZrO_3$/Hap significantly promoted cell growth. The biocompatibility of different coatings can be analyzed by MTT testing, and the results of MTT (methyl thiazolyl tetrazolium) can be used to analyze the toxicity of the coating to cells and the potential for in vivo application, providing a safety assessment for the design of the coating. The MTT assay results for MC3T3-E1 and MSCs further support this conclusion, revealing cellular activities ranging from 131.2 to 156.4% compared with the Control group (Fig. 5b-c). As shown in Figure S6-S9, after US and incubation for 1 Day, we found that the activity of MC3T3 and MSCs cells were at around 41.2% and 53.4%, respectively, which indicated that the ROS generated by the sonodynamic effect of SrTiOZr/Hap were somewhat toxic to the cells, but due to the good biocompatibility of SrTiOZr/Hap, as a large number of cells were still survived. Moreover, after continuing the culture for 3 Day, the activity of MC3T3 and MSCs cells had recovered to 101.4% and 98.7%, respectively, representing that the cytotoxicity of SrTiOZr/Hap treatment was almost nonexistent, and that its ability to promote the cells was able to significantly neutralise the toxic effects of ROS.

Based on the qRT-PCR (Real-Time Quantitative Reverse Transcription Polymerase Chain Reaction) results (Figures S10-S12), we found that SrTiOZr/Hap can promote the expressions of ALP, OPN, and OCN genes after US treatment, which were enhanced about 2.1, 2.9, 1.8-fold compared to PBS treatment. This result illustrated that SrTiOZr/Hap coating is capable of significant osteogenic differentiation after sonication treatment, accelerating the bone repair process without significant toxicity to the cells. Strontium can promote the differentiation and generation of osteoblasts and inhibit osteoclasts from bone resorption. And the piezoelectric effect of the coating can take advantage of the electric field changes caused under the action of ultrasound to influence the behavior of osteoblasts, thus promoting bone repair and regeneration [58, 59]. Hemolysis of the coating was equally critical for in vivo implantation. As depicted in Fig. 5d, Triton X-100 served as the negative control group, while the hemolysis rates of $SrTiZrO_3$, Hap, and $SrTiZrO_3$/Hap were 4.4%, 3.5%, and 3.3%, respectively, all below the standard hemolysis threshold. These suggest that none of these coatings cause hemolysis in vivo, indicating their better biosafety. To investigate the bone-enhancing effects of $SrTiZrO_3$/Hap, transcriptomics analysis was performed. As illustrated in Fig. 5e, treatment with $SrTiZrO_3$/Hap and the US resulted in the up-regulation of 636 genes and the down-regulation of 213 genes, indicating that $SrTiZrO_3$/Hap under the US stimulation modulates gene expression cells. The stability of inter-group differences was subsequently analyzed by PCA (Principal Component Analysis) of the samples, which showed that the significant gene regulation between $SrTiZrO_3$/Hap and Control group (Fig. 5f). As shown in Fig. 5g, the gene expressions of $SrTiZrO_3$/Hap group exhibited significant differences compared to Control, and a multitude of genes related to osteogenesis were found to be up-regulated by heat mapping. Compared with Control, we can find that the $SrTiZrO_3$/Hap group mainly up-regulated the genes such as Gdnf, Lck, Mcf2, Zfp628, and Dcst1, and down-regulated the genes such as Gm45871, Gvin2, Ptprcap, Platr25, Vcan, and Ptp4a1 after US treatment. This was mainly due to the electromagnetic biological effect of US and the piezoelectric effect of $SrTiZrO_3$/Hap (Fig. 5g and Figure S13). Differential gene ontology (GO) classification and enrichment analyzes indicated that $SrTiZrO_3$/Hap primarily affects biological processes, cellular components, and molecular functions. GO enrichment analysis further identified cellular biosynthesis processes as significantly up-regulated (Fig. 5h–k). These differential genes were mainly distributed in the Cellular process, Cell part, and binding, etc. This result suggests that $SrTiZrO_3$/Hap affects the osteogenic differentiation effect of $SrTiZrO_3$/Hap under the action of ultrasound mainly by affecting the cellular process. Through KEGG abundance analysis, we can mine information related to osteogenesis-related metabolic pathways, disease processes, etc., from gene expression data or metabolite abundance data, and gain insights into the molecular mechanisms of osteogenesis of $SrTiZrO_3$/Hap coatings under the action of ultrasound, which is crucial for the resolution of metabolic networks, signaling pathways, and gene regulatory networks [60]. Subsequently, the Kyoto encyclopedia of genes and genomes (KEGG) classification and enrichment analyzes of differentially expressed genes revealed that $SrTiZrO_3$/Hap modulates pathways involved in metabolism, genetic and

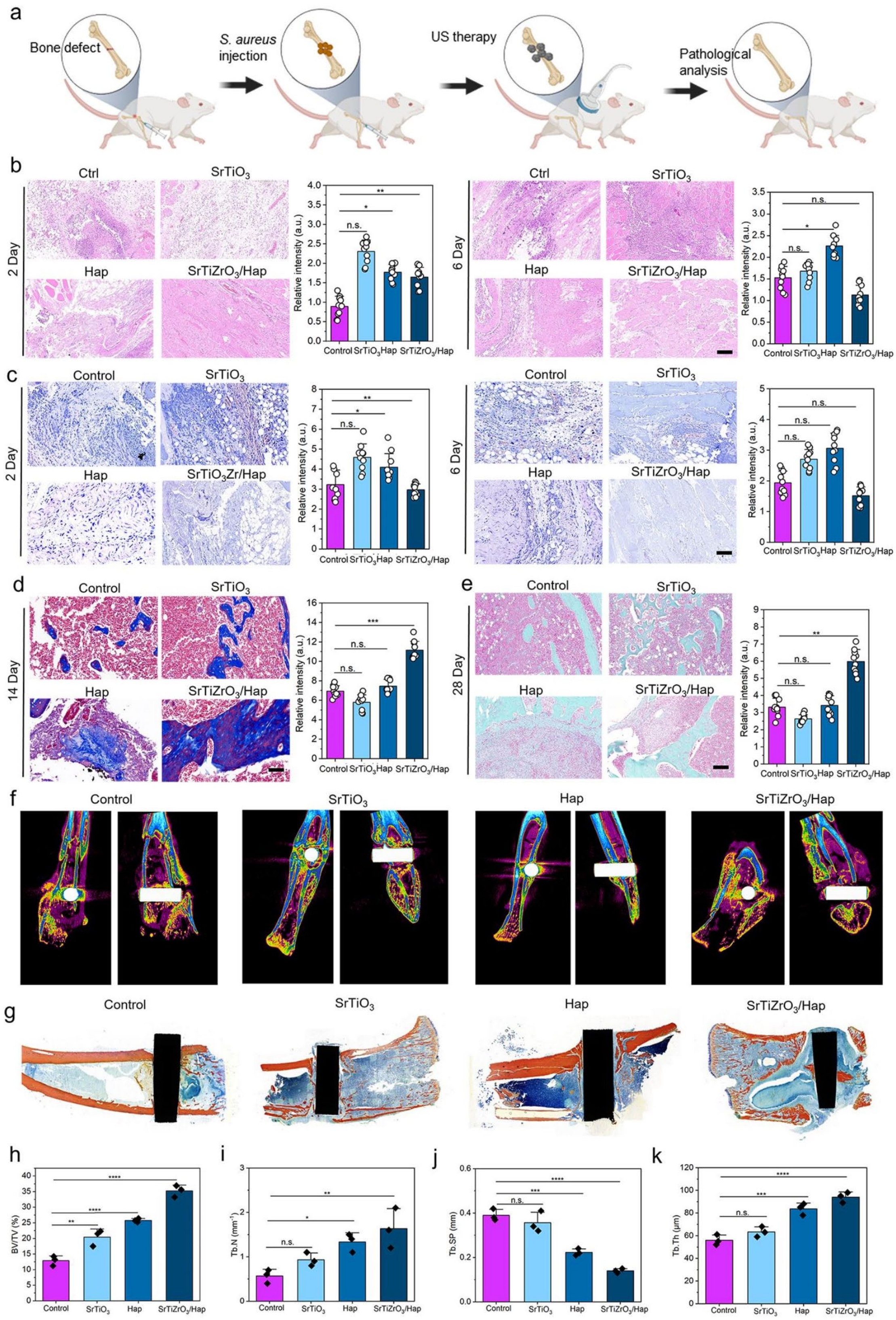

Fig. 6 (See legend on next page.)

(See figure on previous page.)

Fig. 6 **a**, schematic of the therapy process of $SrTiZrO_3$/Hap in the treatment of implant bacterial infection under US irradiation; **b**, the H&E staining of Control, $SrTiO_3$, Hap and $SrTiZrO_3$/Hap after 2 and 6 Day of therapy as well as corresponding calculation, scale bar = 50 μm; **c**, the Giemsa staining of Control, $SrTiO_3$, Hap and $SrTiZrO_3$/Hap after 2 and 6 Day of therapy as well as corresponding calculation, scale bar = 50 μm; **d**, the Masson's stain of Control, $SrTiO_3$, Hap and $SrTiZrO_3$/Hap at infected site after 14 Day of therapy as well as corresponding calculation, scale bar = 50 μm; **e**, the saffron-solid green staining of Control, $SrTiO_3$, Hap and $SrTiZrO_3$/ Hap after 14 Day of treatment as well as corresponding calculation, scale bar = 50 μm; **f**, MicroCT images of Control, $SrTiO_3$, Hap and $SrTiZrO_3$/Hap after 28 days of therapy; **g**, the Hard Tissue Sections of Control, $SrTiO_3$, Hap and $SrTiZrO_3$/Hap after 28 days of therapy; **h**-**k**, calculation of osteogenic quantification of Control, $SrTiO_3$, Hap and $SrTiZrO_3$/Hap after 28 Day of therapy

ToC Figure

environmental information processing, and cellular and oxygenation processes. KEGG enrichment analysis indicated that $SrTiZrO_3$/Hap primarily regulates the PI3K/Akt pathway, facilitating accelerated osteogenic differentiation. This finding is further supported by the enriched chord diagram (Fig. 5l). The PI3K/Akt signaling pathway plays an important role in bone formation, particularly in bone metabolism by regulating the function of osteoblasts. PI3K is activated in response to external stimuli and phosphorylates to produce PIP3 (phosphatidylinositol trisphosphate), which is recruited to activate Akt, which is activated by an upstream kinase that, when activated, can promote osteogenesis by upregulating osteogenesis-related genes (e.g. bone morphogenetic protein OPN, Runx2, etc.). Akt activation promotes osteogenesis by up-regulating osteogenesis-related gene. To evaluate the metalloimmunotherapy activity of $SrTiZrO_3$/Hap, immune response activity against inflammatory cells was tested in vivo (Fig. 5m). CD4 and CD8 are important indicators in immunology and are mainly used to assess the immune function of the organism. By analyzing the immune regulation of CD4 and CD8, the anti-inflammatory effect of $SrTiZrO_3$/Hap coatings can be investigated in vitro and their immunotherapeutic potential can be qualitatively analyzed. In the Control and $SrTiZrO_3$ groups, the CD4/CD8 ratios were 0.07% and 0.19%, respectively, both lower than the 0.32% observed in the $SrTiZrO_3$/Hap group. This suggests that $SrTiZrO_3$/Hap treatment reduced inflammation at the infected site, potentially due to Zr^{4+} release (Figure S14) [61]. Accordingly, the $SrTiZrO_3$/Hap coating can promote bone formation through its piezoelectric effect after US irradiation (Fig. 5n). The therapeutic efficacy of $SrTiZrO_3$/Hap was assessed in vivo using a model of implant-associated bacterial infection. As illustrated in Fig. 6a, bone defects were induced in rats, followed by injection of *S. aureus* to establish infected bone defects. The infected sites were then treated with the US, and pathological sections were analyzed after 14 and 28 days of treatment. H&E staining was a staining method consisting of an alkaline stain, hematoxylin, and an acidic stain, eosin, which was mainly applied to the analysis of the degree of tissue inflammation in this study. Figure 6b presents hematoxylin and eosin (H&E) stained images of the infected bone tissue, revealing significant inflammation in both the Control and the US-treated $SrTiO_3$ and Hap groups at 2 and 6 days, with numerous neutrophils and monocytes observed. After US irradiation, the $SrTiZrO_3$/Hap group exhibited minimal inflammation, mainly caused by residual uncleared *S. aureus*, and the bacteria in the tissues could damage the cellular and extracellular environments of normal tissues. After 6 days of treatment, the inflammation in the $SrTiZrO_3$/Hap group largely disappeared. However, the $SrTiZrO_3$ and Control groups exhibited a significant elevation of inflammation compared with $SrTiZrO_3$/Hap, attributed to the colonization of residual uncleared *S. aureus* in the tissues, which continued to damage the surrounding tissues.

The antimicrobial efficiency of US therapy on infected bone defects was further analyzed using Wright's staining. After 2 days of treatment, the Control, US-treated $SrTiZrO_3$, and Hap groups exhibited numerous bacteria in the infected bone tissues, indicating that the US alone was insufficient in vivo to clear the infection and thus did not demonstrate an antimicrobial effect. A similar phenomenon was observed after 6 days (Fig. 6c). Masson's staining revealed that the $SrTiZrO_3$/Hap group exhibited increased blue collagen after ultrasound treatment, indicating its ability to promote tissue repair around the infection site. This effect is mainly due to the release of calcium ions from the composite structure and its piezoelectric effect under the US, which can promote cell proliferation and differentiation (Fig. 6d). After 28 days of treatment, the osteogenic effect in the Control and the US-treated $SrTiZrO_3$ group was weak, with only a small amount of cartilage production (Fig. 6e). Conversely, the osteogenic effect of $SrTiZrO_3$/Hap was more pronounced compared with Hap, with significant new bone production observed (Figure S15). These results confirmed that $SrTiZrO_3$/Hap exhibited good antimicrobial properties in vivo and excellent osteogenic properties using micro-CT and hard tissue sections. The osteogenic effect of $SrTiZrO_3$/Hap was significantly greater than that of other subgroups, with significant new bone generation around the implant (Fig. 6f–k). As shown in Fig. 6f, it can be found that the final group had the most obvious new bone around the implant, while the Control and $SrTiO_3$ groups had less new bone, a finding that can also be found from Fig. 6g. Based on the hard tissue section images, it can be seen that $SrTiZrO_3$/Hap had the largest amount of bone around the titanium implant, which was significantly higher than that of the $SrTiZrO_3$ and

Hap group. Finally, quantitative calculations from Micro-CT showed that $SrTiZrO_3$/Hap had the highest BV/TV, TB.N, TB.SP and TB.Th, which suggests that it has the highest optimal osteogenesis under US [62]. Calcium ions play a key role in the formation, remodelling and repair of bone. Calcium is not only one of the main components of the bone matrix, but also a key molecule in cell signaling. The piezoelectric effect can promote the directed differentiation of osteoblasts and enhance their mineralisation. External ultrasound can activate intracellular signaling pathways through the piezoelectric effect of $SrTiZrO_3$/Hap, promoting osteoblast proliferation and bone matrix synthesis.

After analyzing the antimicrobial and bone formation properties of the different samples in vivo, we then analyzed their biocompatibility. H&E images of the major organs (heart, liver, spleen, lung, and kidney) of rats after US treatment (Figure S16) revealed that both $SrTiZrO_3$ and $SrTiZrO_3$/Hap did not cause significant tissue damage to these organs after 28 days of implantation in vivo. This finding indicates that neither $SrTiZrO_3$ nor $SrTiZrO_3$/Hap coatings exhibited toxicity to major organs. Therefore, $SrTiZrO_3$/Hap demonstrated good biocompatibility in vivo and excellent antimicrobial and osteogenic abilities under US treatment. We have constructed ultrasound-responsive antibacterial-osteoconductive coatings by means of single-atom doping and construction of heterogeneous interfaces, which are capable of rapidly sterilising and removing bacterial biofilms under ultrasound, and at the same time using piezoelectricity to synergise with ionic release to promote osteogenic differentiation, achieving highly efficient antibacterial and osteoconductive dual functions, which provide new ideas for future orthopaedic implants, restorative materials, and smart medical devices in clinical medicine, with broad application prospects [63]. This provides a new idea for future orthopaedic implants, repair materials and smart medical devices in clinical medicine, and has a wide range of applications.

Conclusions

In this study, $SrTiZrO_3$/Hap coating with US-responsive antimicrobial and osteogenic properties was developed, leveraging single-atom Zr doping and a heterogeneous interface. The needle-like surface topology of $SrTiZrO_3$/Hap can enhance sonodynamic antibacterial activity through physical puncture. The single-atom Zr-doped $SrTiZrO_3$/Hap utilizes released Zr^{4+} ions to modulate immunity, enabling efficient and rapid bacterial clearance through a synergy of puncture-enhanced sonodynamic therapy and metalloimmunotherapy. The mechanism of enhanced piezocatalytic effect was primarily attributed to local interfacial polarization provided by single-atom Zr doping, which can be enhanced by the US to achieve piezo catalysis alongside electronic polarization from the built-in electric field at the heterogeneous interfaces. It can effectively kill *S. aureus* (99.3%) and *E. coli* (99.7%) after US irradiation. It also achieved effective bone tissue repair by regulating the PI3K/Akt pathway and bacterial clearance in an in vivo rat model. These exhibited its potential as a US-responsive antimicrobial, metalloimmunotherapy, and osteogenic coating for implants. This ultrasound-responsive antimicrobial and bone repair treatment strategy has promising applications in orthopaedics, dentistry and other related fields.

Experimental section

Materials

$Sr(NO_3)_2$ (CAS: 10042-76-9, Aladdin), NaOH (CAS: 1310-73-2, Sinopharm), Ti (CAS: 7440-32-6, Macklin), Ca-EDTA (CAS: 23411-34-9, Macklin), KH_2PO_4 (CAS: 7778-77-0, Macklin), $ZrCl_4$ (CAS: 10026-11-6, Macklin), RhB (CAS: 81-88-9, Aladdin), TEMP (CAS: 768-66-1, Aladdin), DCFH-DA kit (CAS: 4091-99-0, Aladdin), crystal violet (CAS: 548-62-9, Beyotime), SYTO9/PI Live and Dead Bacteria Stain Kit (Biotopped, Top0769T), glutaraldehyde (CAS: 111-30-8, Aladdin), acetic acid (CAS: 64-19-7, Aladdin), MTT (CAS: 298-93-1, Solarbio), DMSO (CAS: 67-68-5, Solarbio), EDTA (CAS: 60-00-4, Aladdin), FITC Anti-Mouse CD3 (Biolegend, B369558), PE Anti-Mouse CD4 (Biolegend, B359213), APC Anti-Mouse CD8a (Biolegend, B374670), clostridiopeptidase A (Solarbio, C8160), ACK Lysis Buffer (Solarbio, R1010), PBS Buffer (Solarbio, P1020), HyPure ™Molecular Biology Grade Water (HyClone, SH30538.02), RevertAid First Strand cDNA Synthesis Kit (Thermo, #K1622), FastStart Universal SYBR Green Master (Roche, 4913914001).

$SrTiZrO_3$/Hap preparation

The $SrTiO_3$ coating was prepared by hydrothermal method as follows: the strontium-containing precursor ($Sr(NO_3)_2$, 0.03 M, 40 mL) and NaOH solution (1 M, 10 mL) were stirred for 30 min, and then the mixed solution was slowly transferred to a 100 mL stainless steel reactor with a pure Ti substrate (99%, diameter 6 mm, thickness 2 mm, 0.27 g) placed at the bottom and hydrothermally reacted at 200 ℃ for 24 h. At the end of the reaction, the $SrTiO_3$ samples were taken out and washed with anhydrous ethanol and deionized water for 3 times, and then left to dry at 50 ℃ for 24 h to obtain $SrTiO_3$. For the preparation of the $SrTiZrO_3$, the strontium-containing precursor ($Sr(NO_3)_2$, 0.03 M, 40 mL) and NaOH solution (1 M, 10 mL) were stirred for 30 min, and then 5 mL of $ZrCl_4$ solution with a concentration of 1 mg mL^{-1} was added [64]. This mixed solution was slowly transferred to the bottom of a 100 mL stainless steel reactor and hydrothermally reacted at 200 ℃ for 24 h. After the reaction, the reacted $SrTiO_3$ samples were taken out and washed with anhydrous ethanol and deionized water for 3 times, each time for 5 min, and then left to be dried at 50 ℃ for 24 h to obtain the $SrTiZrO_3$ coating.

Hap preparation

The Hap coating was prepared by hydrothermal method. 30 mL of 0.25 mol L^{-1} Ca-EDTA and KH_2PO_4 solution was mixed and stirring for 30 min. Subsequently, the pH of the mixed solution was adjusted to 8.9 using 4 M NaOH solution and stirring was continued at room temperature for 2 h. After stirring, the mixed solution was slowly transferred to a 100 mL reactor with a substrate (99%, diameter 6 mm, thickness 2 mm, 0.27 g) at the bottom and hydrothermally reacted at 90 ℃ for 20 h. After the reaction was completed, the coated samples were taken out of the reaction and washed three times with anhydrous ethanol and deionized water respectively, and each washing was kept for 5 min. After the reaction, the coated samples were removed and washed 3 times with anhydrous ethanol and deionized water, each time for 5 min, and then left to dry at 50 ℃ for 24 h to obtain the Hap coatings.

SrTiZrO3/Hap preparation

The $SrTiZrO_3$ coating was placed in a precursor solution of 0.25 mol L^{-1} Ca-EDTA and KH_2PO_4, followed by a hydrothermal reaction at 90 ℃ for 20 h. Afterward, the coated samples were removed, washed three times with anhydrous ethanol and deionized water (each wash lasting 5 min), and then dried at 50 ℃ for 24 h to obtain the $SrTiZrO_3$/Hap coating.

Characterization

the surface morphology of the different samples was examined using SEM (ThermoFisher Scientific FEI), where the dried material was first dispersed homogeneously on the conductive adhesive, followed by the removal of any powder that was not firm on the surface in order to prevent it from being sucked into the sample compartment; for the TEM (JEM-F200), the different coatings were scraped and then all configured into a 100 ug mL-1 solution and ultrasonically dispersed for 10 min, then 2 drops were added to the copper mesh and left to dry completely for TEM; for XPS, after drying the samples, the coatings were adhered to the sample trays using conductive adhesive tapes and used for subsequent XPS (AXIS SUPRA) tests.

ROS detection

Regarding to the Rhb degration, different samples were co-cultured with Rhb solution (200 μg mL^{-1}) and then sonicated, and the images of different samples were captured before US and after US treatment. The capture of $^1O_2$ by TEMP leads to the formation of the stable nitrogen-oxygen radical TEMPO, and the rate and concentration changes of singlet oxygen production can be obtained by analysing the EPR signal of TEMPO and combining it with the reaction process [1]. O_2 production was detected by electron spin resonance (ESR) using a TEMP (2,2,6, 6-tetramethyl-4-piperidone hydrochloride) fluorescent probe. The samples were placed in 96-well plates, and then 200 μL of TEMP (50 μg mL^{-1}) probe solution was prepared, and the samples were sonicated for 5 min at 1.0 W cm^{-2}, and the fluorescence values of the probe after sonication were measured by ESR. The ROS production was detected through DCFH-DA probe. Brifely, the different samples were co-cultured with DCFH-DA and then sonicated, and the fluorescence values (excitation wavelength 488 nm, emission wavelength 525 nm) were detected under an microplate reader after 10 min of US.

DFT calculations

The electronic properties of $SrTiO_3$, $SrTiO_3$/Hap, and $SrTiZrO_3$/Hap were analyzed using the generalized gradient approximation of the Perdew–Burke–Ernzerhof exchange-correlation function and pseudopotential plane-wave method. The interactions between ionic nuclei and valence electrons were evaluated using plane-wave ultrasoft pseudopotentials. To ensure convergence accuracy, the plane-wave energy cutoff was set at 450 eV. K-sampling grids for the first irreducible Brillouin zone (BZ) were $8\times8\times8$ for $SrTiO_3$, $6\times6\times5$ for $SrTiO_3$/Hap, and $5\times5\times6$ for $SrTiZrO_3$/Hap, while the k-points for the first BZs of all the heterostructures were set to $3\times3\times1$. Broyden determined the k-points of the first BZs of the heterostructures using the Fletcher–Goldfarb–Shanno algorithm to bring the atoms to their equilibrium positions during the structural relaxation process. For the construction of the $SrTiO_3$, $SrTiO_3$/Hap, and $SrTiZrO_3$/Hap structures, 15 layers of vacuum were added to the C-axis to eliminate the effects of periodicity. Additionally, the convergence tolerance for energy, maximum stress, and maximum displacement were set to 1.0×10^{-5} eV, 0.03 eV $Å^{-1}$, and 0.001 Å, respectively.

Antimicrobial detection

Firstly, all the different coating materials were placed under UV lamp irradiation for 60 min, and then log-phase *S. aureus* and *E. coli* bacterial solution (200 μL, diluted to 10^7 CFU mL^{-1}) were added into 96-well plates containing the coatings and sonicated for 15 min (1.0 W cm^{-2}, 1 MHz), respectively, whereas the groups without US treatment were kept in the dark and left to stand for 15 min. At the end of the antimicrobial process, the bacterial solution were diluted by the same number of times, and then in verted into a 37 ℃ incubator for 24 h. For bacterial fluorescence staining, 1.5 uL of SYTO/9 and PI staining solutions were added to the bacterial solution after antibacterial treatment, and incubated together at room temperature for 20 min. After incubation, fluorescence images of the bacteria were taken under an inverted fluorescence microscope. As for bacterial Resazurin staining, *S. aureus* bacterial solution (200 μL, diluted to 10^7 CFU mL^{-1}) were added into 96-well plates containing the samples and sonicated for 15 min (1.0 W cm^{-2}, 1 MHz), then the bacterial solution was cultured for more time (2 h, 4 h, 6 h, 8 h, 10 h, 12 h, 14 h) with shake cultivation. After antimicrobial process, the solution images were gotten.

Biofilm elimination detection

The bacterial solution of different bacteria was added to a 96-well plate, blown evenly and then placed in a constant temperature incubator at 37 °C for 48 h. The solution was changed every 24 h until a biofilm was formed in the well plate. Subsequently, the prepared coating was added and treated with US (1.0 W cm^{-2}, 1 MHz, 10 min), and after the end of the antibacterial process, the biofilm integrity was evaluated by crystal violet staining after different concentrations of glutaraldehyde (2.5%, v/v, 0.5 mL) were applied to MRSA biofilm for 20 min. Briefly, fixed biofilms were incubated with aqueous crystal violet solution (1% w/v, 0.1 mL) for 5 min and washed three times with PBS. After drying, the remaining crystal violet in the biofilm was dissolved with acetic acid (33% v/v, 0.5 mL), and the corresponding optical density value from 400 to 700 nm was determined by an microplate reader.

MTT detection

MC3T3-E1 and MSCs were co-cultured with $SrTiO_3$, $SrTiZrO_3$, Hap, and $SrTiZrO_3$/Hap for 1 and 3 Day, respectively. After the incubation period, MC3T3-E1 and MSCs activities were evaluated using a MTT kit. After specified incubation times, the cell culture medium was aspirated, and an equal volume of MTT solution (200 μL, 0.5 mg mL^{-1}) was added and then incubated at 37 ℃ for 4 h. After incubation, the MTT solution was aspirated and DMSO was added to terminate the reaction. Absorbance was measured at 490 nm using a microplate reader. Regarding to the cell viability of MC3T3-E1 and MSCs under US treatment, the cells were co-cultured with $SrTiO_3$, $SrTiZrO_3$, Hap, and $SrTiZrO_3$/Hap for 1 and 3 Day, and they were treated through US irradiation at Day 1.

Flow cytometry detection

SD rats weighing approximately 300 g were used and acclimatized for 2 Day. After rearing, 10 μL of *S. aureus* was added to the coated surface and allowed to stand for 20 min. The rats were then anesthetized, and the samples were implanted at the tibia position, followed by US irradiation at 1.0 W cm^{-2} for 20 min. After 2 Day, the flow cytometry of infected tissue was evaluated by using CD4, CD8 antibody.

Transcriptomics assays

MC3T3-E1 was co-cultured with substrate and $SrTiZrO_3$/Hap for 7 days. The $SrTiZrO_3$/Hap group received sonication (1.0 W cm^{-2} for 10 min) at 1, 3, and 5 Day, while the Control group did not undergo sonication. After culture, cells were lysed, and RNA from MC3T3-E1 cells was extracted using an RNA extraction kit. The concentration and purity of the extracted RNA were assessed using a Nanodrop. The transcriptome information of mRNA was then isolated by base pairing with mRNA using magnetic beads. After adding fragmentation buffer, the mRNA fragments were randomly interrupted, and small mRNA fragments of approximately 300 bp were isolated by magnetic bead screening. cDNA was then synthesized by adding six-base random primers for reverse synthesis, ligated with an adaptor, and finally sequenced on the Illumina platform.

Animal experiments

SD rats weighing approximately 300–330 g were used and acclimatized for 2 days. After rearing, 10 μL of *S. aureus* was added to the coated surface and allowed to stand for 20 min. The rats were then anesthetized, and the samples were implanted at the tibia position, followed by US irradiation at 1.0 W cm^{-2} for 20 min and irradiated at day 3. The Control group did not receive ultrasound irradiation. After treatment, the rats were housed and executed at various time points to analyze the in vivo antimicrobial activity of the coating and its promotion of osteogenic repair. The implants were removed after 1 day of treatment and immersed in LB medium for 6 h. A 20 μL sample of the bacterial solution from each group was incubated for 24 h for colony counting. H&E and Wright's staining of bone tissues and peri-bone muscle tissues were performed after 2 and 6 days of continued incubation. Saffron-solid green section staining of bone tissues was performed after 14 and 28 days. H&E staining of the heart, liver, spleen, lungs, and kidneys was performed after 28 days to analyze the in vivo biocompatibility of the different implant coatings.

Statistical analysis

All quantitative data in this study were analyzed using one-way analysis of variance. Each sample was measured in triplicate, and the data are presented as mean ± standard deviation.

The $SrTiZrO_3$/Hap heterojunction coating with single-atom Zr doping and heterogeneous interfaces was designed for ultrasound-responsive antimicrobial and bone formation, which were able to utilize sonodynamic therapy enhanced physical puncture and immune modulation activity of single-atom Zr to kill bacteria efficiently.

Supplementary Information

The online version contains supplementary material available at https://doi.org/10.1186/s12951-025-03309-x.

Supplementary Material 1

Acknowledgements

We thank Home for Researchers editorial team (www.home-for-researchers.com) for language editing service.

Author contributions

X. Zhou, J. Xie, X.C. Zhou, T. Ma: Conceptualization, Methodology, Software; H. Ling, R. Xu: Data curation, Writing-Original draft preparation; D. Kong, Y. Yang, Y. Lu, Z. Xie: Visualization, Investigation; M. Wu, J. Wang, W. Wang, P. Xu: Supervision; H. Xia: Software, Validation; X. Zhou, X. Wan, P. Tong, H. Wu, H. Xia: Writing-Reviewing and Editing.

Funding

This study is founded by the National Natural Science Foundation of China (No. 82260946, No. 82405446, No. 82305266, No.82305279), State-sponsored Postdoctoral Researcher program (GZB20240674), Chinese medicine science and technology project - youth talent supporting program of Zhejiang Province (No. 2025075630), the special talents project of Zhejiang Chinese Medicine University (2023RCZXZK46), the Natural Science Foundation of Jiangxi Province (No. 20212BAB216062), the Chinese Medicine Science and Technology Plan of Jiangxi Province (No. 2021A367).

Data availability

No datasets were generated or analysed during the current study.

Declarations

Ethics approval and consent to participate

All relevant experiments were carried out following the ethical rules enacted by Experimental Animal Ethics Committee in Tianjin (approval code: #SYXK 2021-0003).

Consent for publication

All authors consent to publish.

Competing interests

The authors declare no competing interests.

Author details

[1]The First Affiliated Hospital of Zhejiang Chinese Medical University (Zhejiang Provincial Hospital of Traditional Chinese Medicine), Zhejiang Chinese Medical University, Hangzhou, Zhejiang, China
[2]The First School of Clinical Medicine, Zhejiang Chinese Medical University, Hangzhou, Zhejiang, China
[3]Department of Orthopaedics, Affiliated Hospital of Jiangxi University of Chinese Medicine, Jiangxi University of Chinese Medicine, Nanchang, China
[4]State Key Laboratory of Molecular Engineering of Polymers, Department of Macromolecular Science, Fudan University, Shanghai, P.R. China
[5]Department of Orthopaedics, The People's Hospital of Fengcheng City, Fengcheng, Jiangxi, China
[6]The Graduate School, Jiangxi University of Chinese Medicine, Nanchang, Jiangxi, China
[7]University Medicine Rostock, University of Rostock, Parkstr. 6, 18057 Rostock, Germany
[8]Department of Rehabilitation Medicine, Key Laboratory of Biological Targeting Diagnosis, Therapy and Rehabilitation of Guangdong Higher Education Institutes, The Fifth Affiliated Hospital, Guangzhou Medical University, Guangzhou 510700, China
[9]The First Affiliated Hospital, Zhejiang University School of Medicine, 79 Qingchun Rd., Shangcheng District, Hangzhou 310006, China

Received: 26 September 2024 / Accepted: 8 March 2025

References

1. Qin L, Yang S, Zhao C, Yang J, Li F, Xu Z, Yang Y, Zhou H, Li K, Xiong C, Huang W, Hu N, Hu X. Bone Res. 2024;12(1):28.
2. Masters EA, Ricciardi BF, Bentley KLdM, Moriarty TF, Schwarz EM, Muthukrishnan G. Nat Rev Microbiol. 2022;20(7):385–400.
3. Inzana JA, Schwarz EM, Kates SL, Awad HA. Biomaterials. 2016;81:58–71.
4. Sun M, Lu Y, Zhang H, Jiang W, Wang W, Huang X, Zhang S, Xiang D, Tang B, Chen Y, Chen T, Lian C, Zhang J. Adv Healthc Mater. 2024;13(20):2400346.
5. Lei J, Wang C, Feng X, Ma L, Liu X, Luo Y, Tan L, Wu S, Yang C. Chem Eng J. 2022;435:134624.
6. Li D, Li Y, Shrestha A, Wang S, Wu Q, Li L, Guan C, Wang C, Fu T, Liu W, Huang Y, Ji P, Chen T. Adv Healthc Mater. 2019;8(11):1900002.
7. Lei C, Lei J, Zhang X, Wang H, He Y, Zhang W, Tong B, Yang C, Feng X. Acta Biomater. 2023;172:343–54.
8. Zhang Y, Li Z, Guo H, Wang Q, Guo B, Jiang X, Liu Y, Cui S, Wu Z, Yu M, Zhu L, Chen L, Du N, Luo D, Lin Y, Di P, Liu Y. Adv Sci. 2024;11(26):2310292.
9. Ma L, Cheng Y, Feng X, Zhang X, Lei J, Wang H, Xu Y, Tong B, Zhu D, Wu D, Zhou X, Liang H, Zhao K, Wang K, Tan L, Zhao Y, Yang C. Adv Mater. 2024;36(2):2307846.
10. Hu X, Chen J, Yang S, Zhang Z, Wu H, He J, Qin L, Cao J, Xiong C, Li K, Liu X, Qian Z. Small. 2024:2403681.
11. Fang B, Qiu P, Xia C, Cai D, Zhao C, Chen Y, Wang H, Liu S, Cheng H, Tang Z, Wang B, Fan S, Lin X. Biomaterials. 2021;268:120603.
12. He T, Zhou B, Sun G, Yan Q, Lin S, Ma G, Yao Q, Wu X, Zhong Y, Gan D, Huo S, Jin W, Chen D, Bai X, Cheng T, Cao H, Xiao G. Cell Death Differ. 2024;31(1):90–105.
13. Tang Q, Liu Z, Hu Z-C, Peng H, Wang Z-Y, Liu R-T, Lin Z-H, Zheng Y-Q, Zhang J-S, Zhang C-Q, Wei X-J, Zhu Z-Z. Mater Today Adv. 2023;20:100444.
14. Li J, Han F, Ma J, Wang H, Pan J, Yang G, Zhao H, Zhao J, Liu J, Liu Z, Li B. Adv Funct Mater. 2022;32(10):2111208.
15. Kim J, Park S, Park J-Y, Jung U-W, Jung S, Oh Y, Lee M, Heo S-e, Choi B, Cha J-K, Hong J. Nano Today. 2024;54:102120.
16. Zhang S, Guo Y, Dong Y, Wu Y, Cheng L, Wang Y, Xing M, Yuan Q. ACS Appl Mater Interfaces. 2016;8(21):13242–50.
17. Saint-Pastou Terrier C, Gasque P. J Infect. 2017;75(4):281–92.
18. Liu Y, Wang H, Dou H, Tian B, Li L, Jin L, Zhang Z, Hu L. J Tissue Eng. 2020;11:2041731420930379.
19. Yang J, Chen Z, Gao C, Liu J, Liu K, Wang X, Pan X, Wang G, Sang H, Pan H, Liu W, Ruan C. Nat Commun. 2024;15(1):3565.
20. Liu Y, Li W. Chem. 2019;5(10):2515–7.
21. Yang J, Song L, Shen M, Gou X, Bai L, Wang L, Zhang W, Wu Q, Gong C. Adv Funct Mater. 2021;31(37):2104423.
22. Liu B-T, Pan X-H, Nie D-Y, Hu X-J, Liu E-P, Liu T-F. Adv Mater. 2020;32(48):2005912.
23. Li Y, Liu G, Wang X, Hu J, Liu S. Angew Chem Int Ed. 2016;55(5):1760–4.
24. Wu W, Mao D, Xu S, Kenry; Hu F, Li X, Kong D, Liu B. Chem. 2018;4(8):1937–51.
25. Chen W-H, Zhou Z, Luo G-F, Neumann E, Marjault H-B, Stone D, Nechushtai R, Willner I. Nano Lett. 2019;19(12):9121–30.
26. Son S, Kim JH, Wang X, Zhang C, Yoon SA, Shin J, Sharma A, Lee MH, Cheng L, Wu J, Kim JS. Chem Soc Rev. 2020;49(11):3244–61.
27. Zhang Y, Zhang X, Yang H, Yu L, Xu Y, Sharma A, Yin P, Li X, Kim JS, Sun Y. Chem Soc Rev. 2021;50(20):11227–48.
28. Zhao P-H, Wu Y-L, Li X-Y, Feng L-L, Zhang L, Zheng B-Y, Ke M-R, Huang J-D. Angew Chem Int Ed. 2022;61(5):e202113506.
29. Guan S, Xu W, Tan J, Zhang X, Liu X, Liu L, Qian S, Hou Z, Zhu H, Qiu J, Yeung KWK, Zheng Y, Liu X. ACS Nano. 2024;18(23):15114–29.
30. Wang X, Zhong X, Gong F, Chao Y, Cheng L. Mater Horiz. 2020;7(8):2028–46.
31. Yang Y, Huang J, Liu M, Qiu Y, Chen Q, Zhao T, Xiao Z, Yang Y, Jiang Y, Huang Q, Ai K. Adv Sci. 2023;10(2):2204365.
32. Geng B, Hu J, Li Y, Feng S, Pan D, Feng L, Shen L. Nat Commun. 2022;13(1):5735.
33. Wu J, Huang J, Yu J, Xu M, Liu J, Pu K. Nat Commun. 2025;16(1):153.
34. Yang F, Dong J, Li Z, Wang Z. ACS Nano. 2023;17(5):4102–33.
35. Sun S, Wang D, Yin R, Zhang P, Jiang R, Xiao C. Small. 2022;18(26):2202558.

36. Truong Hoang Q, Ravichandran V, Nguyen Cao TG, Kang JH, Ko YT, Lee TI, Shim MS. Chem Eng J. 2022;435:135039.
37. Yang X, Wang J, El-Sherbeeny AM, AlHammadi AA, Park W-H, Abukhadra MR. Chem Eng J. 2022;431:134312.
38. Bhuin A, Udayakumar S, Gopalarethinam J, Mukherjee D, Girigoswami K, Ponraj C, Sarkar S. Sci Rep. 2024;14(1):10406.
39. Najma B, Kasi AK, Khan Kasi J, Akbar A, Bokhari SMA, Stroe IRC. Appl Surf Sci. 2018;448:104–14.
40. Mendes CR, Dilarri G, Forsan CF, Sapata VdMR, Lopes PRM, de Moraes PB, Montagnolli RN, Ferreira H, Bidoia ED. Sci Rep. 2022;12(1):2658.
41. Wang K, Gao M, Fan J, Huo J, Liu P, Ding R, Li P. ACS Nano. 2024;18(24):16011–26.
42. Liu Z, Ding H, Qi L, Wang J, Li Y, Liu L, Feng G, Zhang L. ACS Appl Mater Interfaces. 2023;15(45):52276–89.
43. Ling J, Wang K, Wang Z, Huang H, Zhang G. Ultrason Sonochem. 2020;61:104819.
44. Kim Y-g, Kim H, Lee G-J, Lee H-U, Lee SG, Baek C, Lee M-K, Park J-J, Wang Q, Cho SB, Jeong CK, Park K-I. Nano Energy. 2021;89:106469.
45. Islam MN, Rupom RH, Adhikari PR, Demchuk Z, Popov I, Sokolov AP, Wu HF, Advincula RC, Dahotre N, Jiang Y, Choi W. Adv Funct Mater. 2023;33(42):2302946.
46. Lee J-H, Park JY, Cho EB, Kim TY, Han SA, Kim T-H, Liu Y, Kim SK, Roh CJ, Yoon H-J, Ryu H, Seung W, Lee JS, Lee J, Kim S-W. Adv Mater. 2017;29(29):1606667.
47. Yang M-M, Zhu T-Y, Renz AB, Sun H-M, Liu S, Gammon PM, Alexe M. Nat Mater. 2024;23(1):95–100.
48. Wang S, Tong W, Li Y, Zhang P, Liu Y, Chen Y, Zhang Y. Nano Energy. 2023;105:108026.
49. Sánchez-Hernández AK, Lozano-Rosas R, Gervacio-Arciniega JJ, Wang J, Robles-Águila MJ. Ceram Int. 2022;48(16):23096–103.
50. Yang J, Du Y, Yao Y, Liao Y, Wang B, Yu X, Yuan K, Zhang Y, He F, Yang P. Adv Sci. 2024;11(13):2307130.
51. Dolai J, Sarkar AR, Maity A, Mukherjee B, Jana NR. ACS Appl Mater Interfaces. 2023;15(51):59155–64.
52. Ghosh S, Sinha M, Samanta R, Sadhasivam S, Bhattacharyya A, Nandy A, Saini S, Tandon N, Singh H, Gupta S, et al. Nat Biomed Eng. 2022;6(10):1180–95.
53. Yin X-L, Li L-L, Li D-C, Wei D-H, Hu C-C, Dou J-M. J Colloid Interf Sci. 2019;536:694–700.
54. Qi K, Zhu W, Zhang X, Liu M, Ao H, Wu X, Zhu Y. ACS Nano. 2022;16(6):9461–71.
55. Li J, Liu X, Tan L, Liang Y, Cui Z, Yang X, Zhu S, Li Z, Zheng Y, Yeung KWK, et al. Small Methods. 2019;3(3):1900048.
56. Bystrov VS, Piccirillo C, Tobaldi DM, Castro PML, Coutinho J, Kopyl S, Pullar RC. Appl Catal Environ. 2016;196:100–7.
57. Song Q, Wang D, Li H, Wang Z, Sun S, Wang Z, Liu Y, Lin S, Li G, Zhang S, et al. Bioac Mater. 2024;32:304–18.
58. Su HL, Chou CC, Hung DJ, Lin SH, Pao IC, Lin JH, Huang FL, Dong RX, Lin JJ. Biomaterials. 2009;30(30):5979–87.
59. Halperin C, Mutchnik S, Agronin A, Molotskii M, Urenski P, Salai M, Rosenman G. Nano Lett. 2004;4(7):1253–6.
60. Xin Y, Jiang J, Huo K, Hu T, Chu PK. ACS Nano. 2009;3(10):3228–34.
61. Yan B, Tan J, Zhang H, Liu L, Chen L, Qiao Y, Liu X. Biomater Adv. 2022;134:112699.
62. Hrabchak C, Rouleau J, Moss I, Woodhouse K, Akens M, Bellingham C, Keeley F, Dennis M, Yee A. Acta Biomater. 2010;6(6):2108–15.
63. Wang Y, Zhang D, Wen C, Li Y. ACS Appl Mater Interf. 2015;7(29):16018–26.
64. Peng L, Yu Y, Gao S, Wang M, Zhang J, Zhang R, Jia W, Sun Y, Liu H. ACS Catal. 2024;14(9):6623–32.

Publisher's note